A new optimization algorithm applied in electromagnetics — Maxwell's equations derived optimization (MEDO)

Donglin SU[1,2,4,5*], Lilin LI[1,3,4], Shunchuan YANG[2,4,5], Bing LI[2,4,5], Guangzhi CHEN[2,4,5] & Hui XU[1,4]

[1]*School of Electronics and Information Engineering, Beihang University, Beijing 100191, China;*
[2]*Research Institute for Frontier Science, Beihang University, Beijing 100191, China;*
[3]*Shenyuan Honors Colledge, Beihang University, Beijing 100191, China;*
[4]*MIIT Key Laboratory of E3 for Smart System and Equipment, Beihang University, Beijing 100191, China;*
[5]*EMC Technology Institute, Beihang University, Beijing 100191, China*

Abstract In this paper, a novel global optimization algorithm, named as Maxwell's equations derived optimization (MEDO), is proposed. Using the Maxwell's equations to analyse the behaviors of the time-varying current, the Ampere force is obtained from Fleming's left hand rule. MEDO introduces an 'Ampere force' term, which is derived from Maxwell's equations and is rigorous in physics, to drive the variables to the global optimal solution in the search space. In addition, introducing 'gravity' to MEDO can increase the stability of the optimizations. 11 classical benchmarks are tested, and results show that MEDO can always converge to numerical optimal solutions. To evaluate the proposed MEDO in solving the electromagnetic problems, four practical engineering applications are considered including the linear antenna array synthesis, frequency selected surface optimization, numerical dispersion reduction for finite-difference method, and parameters extraction of typical waveform. These examples are significant in electromagnetics, but tough to be solved because of their high dimensionality and strong nonlinearity. Numerical results show that MEDO can outperform several classic optimization methods, like wind driven optimization (WDO) and particle swarm optimization (PSO). Therefore, the electromagnetics-inspired MEDO is robust and of great potential in solving the electromagnetic optimization problems.

Keywords electromagnetic theory, heuristic optimization, high-dimensionality, Maxwell's equations, multimodal

1 Introduction

Optimization algorithms, which aim at finding the best solution for a specific problem, like the linear antenna array synthesis and frequency selected surface optimization, are utilized broadly in engineering. In general, optimization algorithms can be divided into three categories: optimization algorithms based on gradient descent, optimization algorithms inspired by nature phenomena, and optimization algorithms derived from physical rules.

The first type includes gradient descent algorithm (GD) [1–4], batch gradient descent (BGD) [5–7], stochastic gradient descent (SGD) [8–10], mini-batch gradient descent (MBGD) [11–13], and so forth.

---

* Corresponding author (email: sdl@buaa.edu.cn)

The principles of these algorithms are based on the mathematical analysis. Once the initial values of the variables are set properly, the optimizations might converge quickly. Thus, they are widely used in the calculation of penalty functions in machine learning. These algorithms depend on the gradient of the objective functions. It can be obtained in machine learning because the penalty function is analytical and derivable. But in most electromagnetic applications, the objective functions are possibly complex or even without analytical expressions, making it difficult to calculate their gradient. Therefore, these optimization methods are limited in electromagnetics.

The second type belongs to heuristic optimizations. Most common algorithms are particle swarm optimizations (PSO) [14,15], genetic algorithms (GA) [16] and their variants. All of them are inspired by natural phenomena, like the foraging behavior of birds and biological genetic phenomenon. Owing to their easy implementation, independence of gradients and strong global search capabilities, they are widely used in various engineering fields [17,18]. In recent years, more and more novel heuristic optimizations have been developed to improve the performance, such as differential evolution (DE) [19,20], the pigeon-inspired optimization [21,22], and ant colony optimization [23,24].

The third type is a special kind of heuristic optimization, which is derived from physical laws and provides a more theoretical basis for the convergence of the iterative formula. One typical representative is wind driven optimization (WDO) [25,26], which describes the motion of air particle through Newton's second law of motion and ideal gas law. Because they do not rely on the mathematical properties of the objective functions, this kind of optimization algorithm is widely used in engineering applications [27,28].

In electromagnetics, the optimization problems are usually high-dimensionality, strong-nonlinearity, and multimodal. In addition, as electromagnetic techniques developed, the accuracy and stability of the optimizations become more and more important for the practical engineering applications. These characters propose high requirements for the performance of the optimization algorithms and pose a challenge to the existing optimization algorithms.

It is wondered that whether we can build an optimization method from the electromagnetic field theory which is more suitable to solve the mentioned electromagnetic problems.

In the electromagnetic field theory, the time-varying electromagnetic fields are coupled to each other, which will produce various effects different from time-invariant fields. This paper focuses on the effect on the current in a coaxial. The current flows back to the source through different pathes when the source frequency of the coaxial varies. We simplify the coaxial to a parallel circuit. The current of the circuit is analysed through the Maxwell's equations and is transformed to be Ampere force through the Fleming's left-hand rule. One part of the conductor in the circuit will explore the search space under the external force. Because the analysis of the current using Maxwell's equations is the basis of the optimization algorithm, we call it Maxwell's equations derived optimization (MEDO).

The rest part of the paper is arranged as follows. Section 2 describes the inspiration and derivation of MEDO in detail, and analyses the computation complexity of MEDO. In Section 3, some typical benchmarks are chosen to verify the performance of the proposed optimization method including accuracy and stability. Section 4 shows four applications of MEDO in electromagnetics. (i) High-dimensional problems: antenna array synthesis and array failure correction. (ii) Optimizations that cannot be expressed by analytic formula: structure design for frequency selective surfaces (FSSs). (iii) Multimodal optimizations: numerical dispersion reduction for finite difference method (FDM). (iv) Optimizations with high requirements for stability: parameters extraction for trapezoidal wave. In Section 5, the advantages and disadvantages of MEDO are concluded, and the potential applications in electromagnetics are indicated for the proposed MEDO method.

2 Formulations of the MEDO

When the electromagnetic fields are time-varying, many different phenomena will be found compared with the static field. One of the typical phenomena in electromagnetic compatibility is that currents must always return to their source, but do not have to return along the predesigned path [29]. It can be
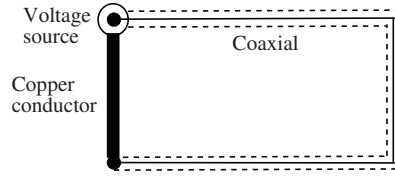
Figure 1 Coaxial model to demonstrate the interesting division of the current. The coaxial is excited by a time-varying source and ended with a matched load. The load and the source are connected by a copper with small impedance.

demonstrated through a simple example.

Let us consider a long coaxial which is excited by a variable frequency source and ended with a matched load. There is a conductor with small impedance to connect the coaxial extremity and a source as shown in Figure 1. Then it can be found that the current follows back to the source through the conductor when the frequency is relatively low. However, in the high frequency region, the current flows back through the outer sheath of the coaxial.

The reason for this phenomenon is that the impedance of the circuit is varied with the frequency, which affects the division of the current in the circuit. Faraday's law shows that a time-varying magnetic field passing through an open surface will induce an electric field, which can form an induced voltage around the contour that encircles the surface. The influence of the induced electric field can be replaced by a loop inductance, which cannot be neglected for the time-varying circuit [29]. Thus, the impedance of the circuit is consisted of the resistance and the inductive reactance: $Z = R + \mathrm{j}\omega L$. When the frequency becomes higher, the impact of the inductive reactance becomes more significant. The impedance of the outer sheath is smaller than that of the conductor under the circumstance, and most of the current will flow back through the sheath. As for a time-invariant situation, electric and magnetic fields are decoupled, and the impedance just refers to the resistance, expressed as $Z = R$. The resistance of the copper conductor is much smaller than the outer sheath. Thus, most of the current flows back through the copper conductor when the source is time-invariant [30].

In this paper, we focus on the phenomenon that the current loop has changed because of the time-varying effect. We analyse the current through the Faraday's law and the law of conservation of charge in Maxwell's equations, and build an optimization algorithm based on it. The single dimension situation is discussed firstly.

To simplify the coaxial model, it can be regarded as a parallel circuit, where the two branches are the conductor and the outer sheath, respectively. As analysed above, in a time-varying circuit, the total impedance of the circuit consists of two parts: one part is the self-resistance which depends on the material, length, and cross sectional area of the conductor; the other part is the inductive reactance which depends on the frequency and loop area of the circuit. As for the circuit with two branches paralleled, the division of the current on the two branches is impacted by the impedance, which is related to the frequency of the source, the self-resistance of the conductor on the two branches, and the loop area of each branch.

In order to adapt to the construction of the optimization algorithm, some modifications of the previous coaxial model in Figure 1 have been done as shown in Figure 2. In the parallel circuit, AKG is the main branch. $ACDFGK$ constitutes the current loop 1, with small resistance and large loop inductance. It can be regarded as the copper conductor in the coaxial modal. $AJIHGK$ constitutes the current loop 2, whose resistance is large and loop inductance is small. It is analogous to the outer sheath of the coaxial. We focus on one segment in the loop 2, which is marked as GH in Figure 2. We consider GH as an individual to find the optimal solution of the objective function, allow the position of GH variable, and call it 'slide bar'. We treat the curve HI as the region to be optimized, which is of the same shape of the objective function. To move the slide bar, the circuit is placed in a constant magnetic field. According to the analysis above, given the value of the voltage source, the current on the slide bar can be calculated. Assuming that the direction of magnetic field is perpendicular to and pointing into the paper, and the voltage source is assigned to be equal to the negative gradient of the objective function, then the slider will move toward the minimum point of the objective function driven by Ampere force and gravity. The
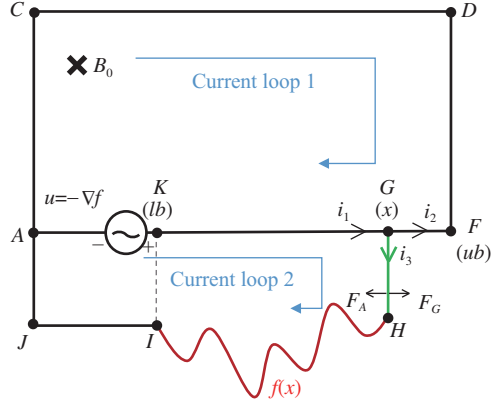
Figure 2 (Color online) Schematic of MEDO. The schematic is divided into several segments. AKG is the main branch of the circuit, whose impedance is marked as Z_1. $ACDFGK$ is the paralleled branch in current loop 1, and $AJIHGK$ is the paralleled branch in current loop 2. Their impedances are recorded as Z_2 and Z_3. GH is the individual in the optimization algorithm whose task is to find the optimal solution. Point G is the position of the individual, which is known as variable of the optimization question. KF is the domain of the variable, whose minimum and maximum values are denoted as *lb* and *ub*. HI is the area to be optimized. F_G and F_A refer to the external force acting on GH, which will be introduced in detail in the body.

detailed analysis is introduced below.

To simplify the analysis, all of the curves in Figure 2 are regarded as conductors, whose cross sectional area and resistivity are supposed to be 1. Therefore, the self-resistance of the conductors is only related to their length.

2.1 Ampere force F_A

Ampere force on GH can be expressed as

$$F_A = i_{GH} B_0 L, \tag{1}$$

where L is the length of slide bar, B_0 is the magnetic flux density, whose positive direction is perpendicular into the paper, i_{GH} is the current on slide bar GH. The key to evaluate F_A is to calculate the current on the slide bar i_{GH}. To derive i_{GH} in detail, we firstly define some symbols of different currents in the circuit and the forward direction of the currents:

i_1. Current on the main branch, the forward direction of i_1 is $K \to G$.

i_2. Current on the loop 1, the forward direction of i_2 is $G \to F \to A$.

i_3. Current on the loop 2, which is i_{GH}. The forward direction of i_3 is $G \to H$.

2.1.1 *Law of conservation of charge*

When slide bar GH is located at a position x_{cur}, i_2 and i_3 can be calculated through law of conservation of charge:

$$i_2 + i_3 - i_1 = \Sigma i = \oint \boldsymbol{J} \cdot \mathrm{d}\boldsymbol{a} = -\frac{\mathrm{d}}{\mathrm{d}t} \int \rho \mathrm{d}V = -\frac{\mathrm{d}}{\mathrm{d}t} Q_{\mathrm{net}} = -\frac{\mathrm{d}}{\mathrm{d}t} C_A V(t). \tag{2}$$

Considering that node capacitance C_A is always ignored, Eq. (2) can be simplified as

$$i_2 + i_3 = i_1, \tag{3}$$

where i_1 can be calculated from Ohm law:

$$i_1 = \frac{u}{Z_{\mathrm{total}}}, \tag{4}$$

where u is related to the voltage source. In order to make the slide bar move towards the minimal point, we set the voltage source as the negative gradient of the objective function at the current point, which is

similarly calculated by the difference of the current point and its adjacent point. Z_{total} refers to the total impedance in the circuit including the main branch impedances Z_1, and paralleled branch impedances Z_2, Z_3. As the source is time-varying, we need to consider not only the resistance, but also the loop inductance. In order to simplify the problem, we consider the loop inductances just in two branches. Consequently, the total impedance can be derived from

$$Z_{\text{total}} = Z_1 + \frac{Z_2 Z_3}{Z_2 + Z_3} = R_1 + \frac{Z_2 Z_3}{Z_2 + Z_3}, \tag{5}$$

where

$$Z_2 = R_2 + Z_{L2}, \tag{6}$$

$$Z_3 = R_3 + Z_{L3}. \tag{7}$$

In calculation of Z_{L2} and Z_{L3}, some specialties are used. Generally, the induced voltage on the inductor is proportional to the rate of change of current in the inductor, as follows:

$$u = L\frac{\mathrm{d}i}{\mathrm{d}t}. \tag{8}$$

According to Ohm's law, the loop inductive reactance Z_{L2} and Z_{L3} can be obtained as

$$Z_{L2} = \frac{L_2}{i_2}\frac{\mathrm{d}i_2}{\mathrm{d}t}, \tag{9}$$

$$Z_{L3} = \frac{L_3}{i_3}\frac{\mathrm{d}i_3}{\mathrm{d}t}. \tag{10}$$

2.1.2 Faraday's law

On the other hand, according to the Faraday's law, the integral of the E-field along the path $ACDFGHJ$ can be expressed as

$$\oint \boldsymbol{E} \cdot \mathrm{d}\boldsymbol{s} = -\frac{\mathrm{d}}{\mathrm{d}t}\int \boldsymbol{B} \cdot \mathrm{d}\boldsymbol{a} = -\frac{\mathrm{d}}{\mathrm{d}t}\Phi = -B_0\frac{\mathrm{d}}{\mathrm{d}t}S_{CDHJ}, \tag{11}$$

where $\frac{\mathrm{d}}{\mathrm{d}t}S_{CDHJ}$ refers to the area enclosed by path $ACDFGHJ$. Furthermore, the integral on the left side of the equation can be calculated by the sum of voltage across each element in the loop:

$$\oint \boldsymbol{E} \cdot \mathrm{d}\boldsymbol{s} = \sum_{i=1}^{n} V_i = i_2 Z_2 - i_3 Z_3. \tag{12}$$

After combining (11) and (12), the relation of i_2 and i_3 can be obtained as

$$i_2 Z_2 - i_3 Z_3 = -B_0\frac{\mathrm{d}S_{CDHJ}}{\mathrm{d}t}. \tag{13}$$

The current on the slide bar can be solved through (2) and (13):

$$i_3 = \frac{\frac{u}{Z_{\text{total}}}Z_2 + B_0\frac{\mathrm{d}S}{\mathrm{d}t}}{Z_2 + Z_3}. \tag{14}$$

Ampere force F_A can be calculated by (1) and (14).

However, R_3, L_3, and $\frac{\mathrm{d}S_{CDHJ}}{\mathrm{d}t}$ in (7) and (13) are difficult to be determined, which will be explained in detail below.

(1) R_3. R_3 refers to the paralleled branch resistor in current loop 2, which is consist of line segment AJ, JI, GH, and curve HI. The value of R_3 is proportional to the total length of AJ, JI, GH, and HI. The difficulty of the expression of R_3 is the length of curve HI, which is approximately substituted by straight lines, as shown in Figure 3(a). In order to reduce the difference between the maximum and minimum
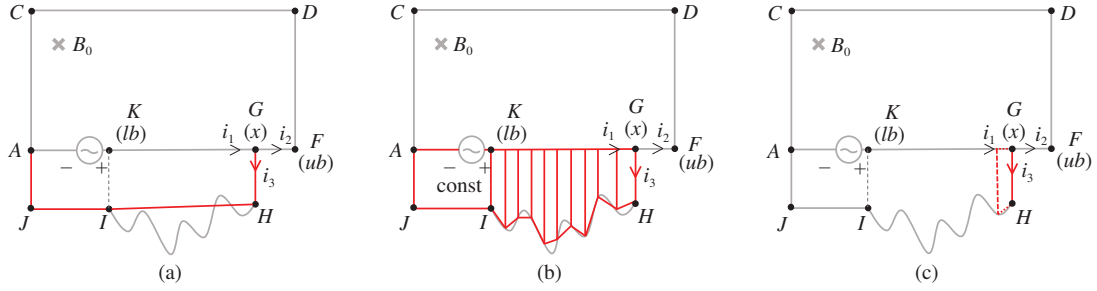
Figure 3 (Color online) Schematic diagram of calculating. (a) R_3; (b) L_3; and (c) $\frac{\mathrm{d}S_{CDHJ}}{\mathrm{d}t}$.

values of the objective function in each iteration, the values of the objective function are normalized by the max value obtained by the individuals. Then R_3 can be calculated by

$$R_3 = \mathrm{const}1 + (1 - f(\boldsymbol{x}_{j,\mathrm{cur}})) + \sqrt{(\boldsymbol{x}_{j,\mathrm{cur}} - \boldsymbol{lb})^2 + (f(\boldsymbol{x}_{j,\mathrm{cur}}) - f(\boldsymbol{lb}))^2}, \tag{15}$$

where $\boldsymbol{x}_{j,\mathrm{cur}}$ refers to the current position of the jth individual. const1 is a constant, which represents the resistance of AJI, and is independent of the objective function. According to the configurations, const1 should be assigned to a very small number, whose default value is 0.1 in our simulations.

(2) L_3. L_3 refers to loop inductance owing to loop 2. Generally, the value of the loop inductance is proportional to the area of the loop. To simply the calculation, the proportionality factor is noted to be 1. Thus, L_3 can be approximated by the area of loop 2, which is instituted by the sum of multiple small trapezoids, as shown in Figure 3(b).

$$L_3 = \mathrm{const}2 + \sum_{j=1}^{\mathrm{popsize}} \left\{ (1 - f(\boldsymbol{x}_{j,\mathrm{cur}}) + 1 - f(\boldsymbol{x}_{j+1,\mathrm{cur}})) \times (\boldsymbol{x}_{j+1,\mathrm{cur}} - \boldsymbol{x}_{j,\mathrm{cur}}) \div 2 \right\}, \tag{16}$$

where popsize refers to the number of individuals in MEDO, which is set by users. const2 is another constant, which represents the area of rectangle $AJIK$. Because we mainly consider the effect of the objective function on the area of loop 2, here we can set const2 to a very small value, such as 0.1.

(3) $\mathrm{d}S_{CDHJ}/\mathrm{d}t$. $\mathrm{d}S_{CDHJ}/\mathrm{d}t$ refers to the rate of change of the area enclosed by path $ACDFGHJ$ over time, which is approximately represented by a trapezoid, as shown in Figure 3(c). $\mathrm{d}t = 1$ is assumed in this paper to simplify the analysis.

$$\frac{\mathrm{d}S}{\mathrm{d}t} = \Delta S = \frac{(1 - f(\boldsymbol{x}_{j,\mathrm{cur}}) + 1 - f(\boldsymbol{x}_{j,\mathrm{new}})) \times (\boldsymbol{x}_{j,\mathrm{new}} - \boldsymbol{x}_{j,\mathrm{cur}})}{2}. \tag{17}$$

2.2 Gravity $\boldsymbol{F}_G$

In order to enhance the robustness of the algorithm, gravity is factitiously appended here to the model. The definition of gravity is reaffirmed first of all, which is defined as the force pulling the slide bar from its current location towards the center of the coordinate system [25]. The vector $\boldsymbol{g}$ is written as $\boldsymbol{g} = |\boldsymbol{g}|(-\boldsymbol{x}_{\mathrm{cur}})$, and the gravity can be expressed as

$$\boldsymbol{F}_G = m|\boldsymbol{g}|(-\boldsymbol{x}_{\mathrm{cur}}), \tag{18}$$

where m refers to the weight of the slide bar. $(-\boldsymbol{x}_{\mathrm{cur}})$ refers to the distance from the current position to the center, which means that the further the sliding bar is from the center, the greater the gravity.

2.3 Law of motion according to momentum theorem

Above all, under the push of Ampere force and gravity, the slide bar will move following momentum theorem:

$$m\boldsymbol{v} = (\boldsymbol{F}_A + \boldsymbol{F}_G)t, \tag{19}$$

where m is the quality of the slide bar, which can be calculated by $m = \rho L S_{\text{bar}}$, where ρ is the density of the slide bar, L is the length, and S_{bar} is the sectional area, respectively. v is the speed of the slide bar, which can be computed by the position difference between two near-by iterations: $\boldsymbol{v}_{\text{new}} = \frac{\mathrm{d}\boldsymbol{x}}{\mathrm{d}t} = \boldsymbol{x}_{\text{new}} - \boldsymbol{x}_{\text{cur}}$. $\boldsymbol{F}_A + \boldsymbol{F}_G$ is the total force applied to the slide bar, which can be obtained by (1) and (18). t is the time duration from the starting to current, represented by the number of iterations.

Above all, the slide bar's motion law can be simplified and rewritten, and the final iterative formula of MEDO is obtained as

$$v_{\text{new}} = \left(\frac{B_0}{\rho S_{\text{bar}}} i_3 - (x_{\text{last}} + v_{\text{cur}}) |g| \right) \cdot \text{iter}, \tag{20}$$

$$x_{\text{new}} = x_{\text{cur}} + v_{\text{new}} \cdot \Delta t. \tag{21}$$

Eq. (20) can be further simplified to be

$$v_{\text{new}} = -|g| \cdot \text{iter} \cdot v_{\text{cur}} + \left(\frac{B_0}{\rho S} i_3 - x_{\text{last}} \right) \cdot \text{iter}. \tag{22}$$

2.4 Explanations of MEDO and coefficients in MEDO

In each iteration, the force to drive the slide bar is divided into two parts. One is the Ampere force $\boldsymbol{F}_A$. The direction of Ampere force points to the direction in which the gradient of the objective function decreases. The other one is the gravity $\boldsymbol{F}_G$. The direction of gravity points to the coordinate origin, which can help the slide bar to skip the local minimal point. In addition to the gradient, the function values of other individuals and the function values of the last iteration are also used in the calculation of $\boldsymbol{F}_A$. Then, the proposed MEDO can find the minimal position of the objective functions.

There are 5 coefficients that need to be determined to start an optimization, namely: $|\boldsymbol{g}|$, B_0, ρS_{bar}, R_1, L_2. From (20)–(22), it can be inferred that MEDO is an optimization algorithm that must converge within a limited number of iterations. Otherwise, as the number of iterations goes to infinity, x_{new} will also go to infinity and the algorithm will diverge. In consequence, we define the 'effective number of iterations', which is denoted by M. The premise that MEDO can accurately converge is to choose appropriate value of the 5 coefficients so that in the range of iter $< M$, the speed v tends to 0, and the position of the slide bar tends to remain unchanged. Then, the MEDO can find the optimal value of the objective function.

In order to ensure the convergence of the algorithm, we give a rough approximate range of each coefficient according to the physical meaning of the model and numerical experiments.

(1) $|g|$. Its physical meaning is gravity acceleration. According to (22), the range of $|g|$ should meet $|-|g| \cdot \text{iteration}| < 1$. Because it is necessary to achieve convergence within the effective number of iterations M, we have iteration $< M$. So the range of $|g|$ is $|g| < \frac{1}{M}$. To ensure the convergence of MEDO, the value range of M is generally greater than 200. Thus, the value range of $|g|$ can be further refined to $|g| \leqslant 0.005$.

(2) B_0. In order to ensure that Ampere force points to the direction in which the gradient of the objective function decreases, B_0 should be perpendicular into the paper surface, resulting in $B_0 \geqslant 0$. According to (14) , if the value of B_0 is small, the positive and negative of i_3 is more likely to be consistent with the voltage u. It is a necessary condition that the Ampere force points to the direction of the negative gradient. Therefore, B_0 should take a positive number with a smaller absolute value, generally less than 5.

(3) ρS_{bar}. It represents the per-unit-length weight of the slide bar. According to the second part in the iterative formula, ρS_{bar} should take a large number to prevent the slide bar from exceeding the domain of the function as the iteration increases. Our numerical experiments show that $\rho S_{\text{bar}} \geqslant 200$ is suitable for most applications.

(4) R_1. It is the resistant of main branch, which is related to the calculation of i_3. In order to keep the positive and negative of i_3 as consistent as possible with voltage u, $R_1 \gg 0$ is required. Generally, we require $R_1 \geqslant 500$.

(5) L_2. It is the loop inductance of current loop 1, which is related to the calculation of i_3. According to Figure 2, loop 1 has a large loop inductance. Thus, L_2 is generally a large value. According to amounts of numerical experiments, the range of L_2 has reached to be 10^5 and larger.

The pseudocode of MEDO is illustrated in Algorithm 1.

Algorithm 1 Time-varying effect optimization

Require: $\min f_{\text{objective}}(x)$;
 1: Preset: objective function, population size, maximum iterations;
 2: Preset: $|g|$, B_0, ρS_{bar}, R_1, L_2;
 3: Initialization: x_0, v_0;
 4: **while** iter < maximum number of iterations **do**
 5:    Calculate $f_{\text{objective}}(x)$;
 6:    $u = -\nabla f(x)$;
 7:    Calculate Z_{total}, Z_2, Z_3, $\frac{\mathrm{d}S}{\mathrm{d}t}$;
 8:    $i_3 = \frac{\frac{u}{Z_{\text{total}}}Z_2 + B_0 \frac{\mathrm{d}S}{\mathrm{d}t}}{Z_2 + Z_3}$;
 9:    $v_{\text{new}} = -g \cdot \text{iter} \cdot v_{\text{cur}} + (\frac{B_0}{\rho S}i_3 - x_{\text{last}}) \cdot \text{iter}$;
10:    $x_{\text{new}} = x_{\text{cur}} + v_{\text{new}}$;
11:    **if** $|x_{\text{new}} - x_{\text{cur}}| <$ threshold **then**
12:       Exit.
13:    **end if**
14: **end while**

2.5 Computation complexity analysis

2.5.1 *Time complexity analysis*

For each iteration, the computations required for MEDO mainly contain the calculations of the objective functions and their gradient. Use M to represent the maximum number of iterations, P to represent the population size, and D to represent the dimension of the objective function. Then, the objective function need to be calculated for $(PM + 2DPM)$ times in the whole iteration. Besides, the time complexity of evaluating the objective function is related to the particular objective function under consideration, whose time complexity can be denoted as $O(f)$. Thus, the time complexity of MEDO can be expressed as $O(DPM) \times O(f)$.

Similarly, if the gradient in GD is calculated by the difference method, then the time complexity of GD is $O(DM) \times O(f)$, and the time complexity of PSO is $O(PM) \times O(f)$. It can be found that the time complexity of MEDO is larger than GD and PSO, which is because that the gradient information is approximately calculated by using the difference method for each individual in MEDO.

2.5.2 *Space complexity analysis*

Space complexity measures the amount of working storage that MEDO needs. As time complexity, we express this conception in big-Oh terms without considering the low-order terms and the first-term coefficients. The main variables in MEDO are the values of the objective functions, the positions of the individuals and the velocities of the individuals, with the memory need of P units, $D \times P$ units and $D \times P$ units, respectively. As a result, the space complexity of MEDO can be expressed as $O(DP)$.

Similarly, the space complexity of GD is $O(D)$, and the space complexity of PSO is $O(DP)$.

2.6 Multidimensional situations

Multidimensional cases can be extended directly from the iterative formula by replacing the position x to the multidimensional vector $\boldsymbol{x}$. In detail, a multidimensional problem can be treated as a series of parallel searches that every model is working to find the optimal variable in one dimension. After each iteration, the variables obtained by each model are jointly calculated to obtain the value of the current objective function.

Table 1 Description of 11 benchmark functions

Function	Range	Dimension	$F_{\min}$
$F_1 = \sum_{i=1}^{n} (x_i - 2)^2$	$[-10, 10]$	40	0
$F_2 = \sum_{i=1}^{n} |x_i| + \prod_{i=1}^{n} |x_i|$	$[-10, 10]$	40	0
$F_3 = \sum_{i=1}^{n} \left(\sum_{j=1}^{i} (x_j) \right)^2$	$[-100, 100]$	40	0
$F_4 = \sum_{i=1}^{n} |x_i + 0.5|^2$	$[-100, 100]$	40	0
$F_5 = \text{random}[0, 1) + \sum_{i=1}^{n} i x_i^4$	$[-1.28, 1.28]$	40	0
$F_6 = \sum_{i=1}^{n} \left[x_i^2 - 10 \cos(2\pi x_i) + 10 \right]$	$[-5.12, 5.12]$	40	0
$F_7 = -20 \exp(-0.2 \sqrt{\frac{1}{n} \sum_{i=1}^{n} x_i^2}) - \exp\left(\frac{1}{n} \sum_{i=1}^{n} \cos(2\pi x_i)\right) + 20 + e$	$[-32, 32]$	40	0
$F_8 = \frac{1}{4000} \sum_{i=1}^{n} x_i^2 - \prod_{i=1}^{n} \cos\left(\frac{x_i}{\sqrt{i}}\right) + 1$	$[-600, 600]$	40	0
$F_9 = [1 + (x_1 + x_2 + 1)^2 \left(19 - 14x_1 + 3x_1^2 - 14x_2 + 6x_1 x_2 + 3x_2^2\right)]$ $\times [30 + (2x_1 - 3x_2)^2 \times \left(18 - 32x_1 + 12x_1^2 + 48x_2 - 36x_1 x_2 + 27x_2^2\right)]$	$[-2, 2]$	2	3
$F_{10} = 0.5 + \frac{\sin^2(x_1^2 - x_2^2) - 0.5}{(1 + 0.001(x_1^2 + x_2^2))^2}$	$[-100, 100]$	2	0
$F_{11} = -0.5 + \frac{\sin^2 \sqrt{x_1^2 + x_2^2}}{(1 + 0.001(x_1^2 + x_2^2))^2}$	$[-100, 100]$	2	-1

Table 2 Values of the coefficients of MEDO when calculating different benchmark functions

Function	B_0	ρS	$|g|$	R_1	L_2
F_1	2	5E + 2	2E − 3	1E + 6	3E + 9
F_2	0	5E + 2	2E − 3	1E + 2	3E + 9
F_3	0	5E + 2	2E − 3	1E + 2	3E + 9
F_4	5E − 1	5E + 2	2E − 3	3E + 2	3E + 9
F_5	0	1E + 3	8E − 4	3E + 6	8E + 9
F_6	1.16E − 9	5.63E + 2	2E − 3	1E + 3	3E + 9
F_7	0	5E + 2	2E − 3	5E + 2	3E + 9
F_8	0	5E + 2	2E − 3	5E + 2	3E + 9
F_9	1.4	9E + 3	3E − 5	5E + 2	3E + 9
F_{10}	2.8E − 8	2.32E + 2	5E − 3	5.1E + 2	3E + 5
F_{11}	1E − 1	2E + 2	5E − 3	5E + 2	3E + 5

3 Benchmarks

3.1 Test functions and test environment

In order to evaluate the convergence and accuracy of the MEDO, 11 benchmark functions have been tested. Functions F_1–F_5 are unimodal functions which can test the ability of the algorithm to converge to the minimum in general. Functions F_6–F_{11} are multimodal functions which can test the ability of the algorithm to jump out of the local optimum.

Function expressions and variable range are shown in Table 1. The 5 coefficients in this part are chosen according to Subsection 2.4 and shown in Table 2.

Every function has been run for 100 times, 500 iterations every time starting from different populations randomly generated. The population size is set as 40. Statistical results including average value and variance are shown in Tables 3 and 4. To fairly compare the performance between MEDO and other optimizations, several typical algorithms have been tested in the same environment, such as adaptive wind driven optimization (AWDO), PSO, DE and GD. All the tests are completed on the Inter Core(TM) i5-8250U CPU@1.6 GHz, MATLAB R2017a.

3.2 Results and discussion

Tables 3 and 4 show the average and variance of convergence results calculating by different optimization algorithms. In general, the value of the average can represent the convergence accuracy of the algorithm.

Table 3 Comparison of the average of optimization results between MEDO, AWDO, PSO, DE, and GD

Function	MEDO	AWDO	PSO	DE	GD
F_1	2.06E − 10	8.10E − 09	1.159299	0.356657	**0**
F_2	**0**	**0**	14156.03	4.753654	1E + 38
F_3	**0**	**0**	5.95349	36.35761	8.16E − 9
F_4	2.39E − 16	5.88E − 10	6.799546	36.06591	**1.94E − 27**
F_5	**6.08E − 05**	6.80E − 05	65.75983	0.281079	22.54327
F_6	**0**	**0**	181.557	320.1764	350.34270
F_7	**8.88E − 16**	**8.88E − 16**	20.25262	2.878327	19.50377
F_8	**0**	**0**	753.0833	1.349412	1.05304
F_9	3.0001	3.0001	3.008	**3**	144.95598
F_{10}	**0**	**0**	1.78E − 08	0	0.50283
F_{11}	**−0.9999997**	−0.99922	−0.99998	−0.9966	−0.53942

Table 4 Comparison of the variance of optimization results between MEDO, AWDO, PSO, DE, and GD

Function	MEDO	AWDO	PSO	DE	GD
F_1	2.56E − 19	1.73E − 15	0.094204	0.051561	**0**
F_2	**0**	**0**	1.99E + 11	2.700029	1E + 78
F_3	**0**	**0**	54.079	421.2083	1.50E − 18
F_4	1.16E − 32	2.74E − 18	42.17984	361.9966	**3.61E − 55**
F_5	**4.20E − 09**	4.84E − 09	1891.318	0.008171	2079.07924
F_6	**0**	**0**	1477.551	356.0968	2886.41731
F_7	**0**	**0**	0.117238	0.172126	0.01412
F_8	**0**	**0**	1954.504	0.039167	5.29E − 5
F_9	1.81E − 8	1.34E − 06	0.000105	**8.05E − 31**	80171.13443
F_{10}	**0**	**0**	3.42E − 16	**0**	0.00179
F_{11}	**6.59E − 14**	7.02E − 06	3.53E − 10	2.17E − 05	0.00708

Average values that are closer to the minimum represent higher accuracy. Meanwhile, the value of the variance can represent the stability. The smaller variance means the higher stability. In Tables 3 and 4, the best results are shown in bold fonts.

Some results obtained by PSO, DE, and GD have relatively large errors. The reason might be that the dimension of F_1–F_8 is set to be 40. The high dimension increases the difficulty of finding the optimal value for PSO, DE, and GD, and leads to the error accumulation. Particularly, the result obtained by GD for F_2 might be out of normal expectations. It is because that the gradient of F_2 increases linearly with the dimension grows. When the dimension of the function is 40, its gradient is extremely large, causing the variable to cross the boundary quickly. Therefore, even if the learning rate has been set as 10^{-23}, the result still cannot converge. Besides, when solving the multi-modal functions, GD might fall into the local optimal solution as shown in Tables 3 and 4.

Furthermore, in order to verify the applicability of optimization algorithms to higher dimensional problems, some additional tests have been done. In benchmark cases, dimensions of functions F_1–F_8 are variable. Thus, a scan from 10-dimension to 100-dimension is set to analyse the variation of the accuracy of different optimization algorithms with dimension increases. Figure 4 shows the results of MEDO and three other optimizations when dealing with above situations for functions F_1–F_8. In Figures 4(b), (f), and (g), the optimal results of MEDO and AWDO are always 0 with the increase of dimensions. As a result, no locally enlarged images are specifically drawn in these subgraphs. Especially, GD is not tested for function F_2 because it cannot convergence normally.

From the results of the benchmark tests, it is confirmed that MEDO can converge to the minimum point of the objective functions with a satisfying value. Compared with AWDO, PSO, DE, and GD, the optimization results of MEDO are more accurate and stable in most instances. In addition, with the dimensions of the optimization increase, the convergence accuracy of other optimization algorithms decreases to some extent, whereas the result of MEDO still keeps accurate. In consequence, MEDO is a
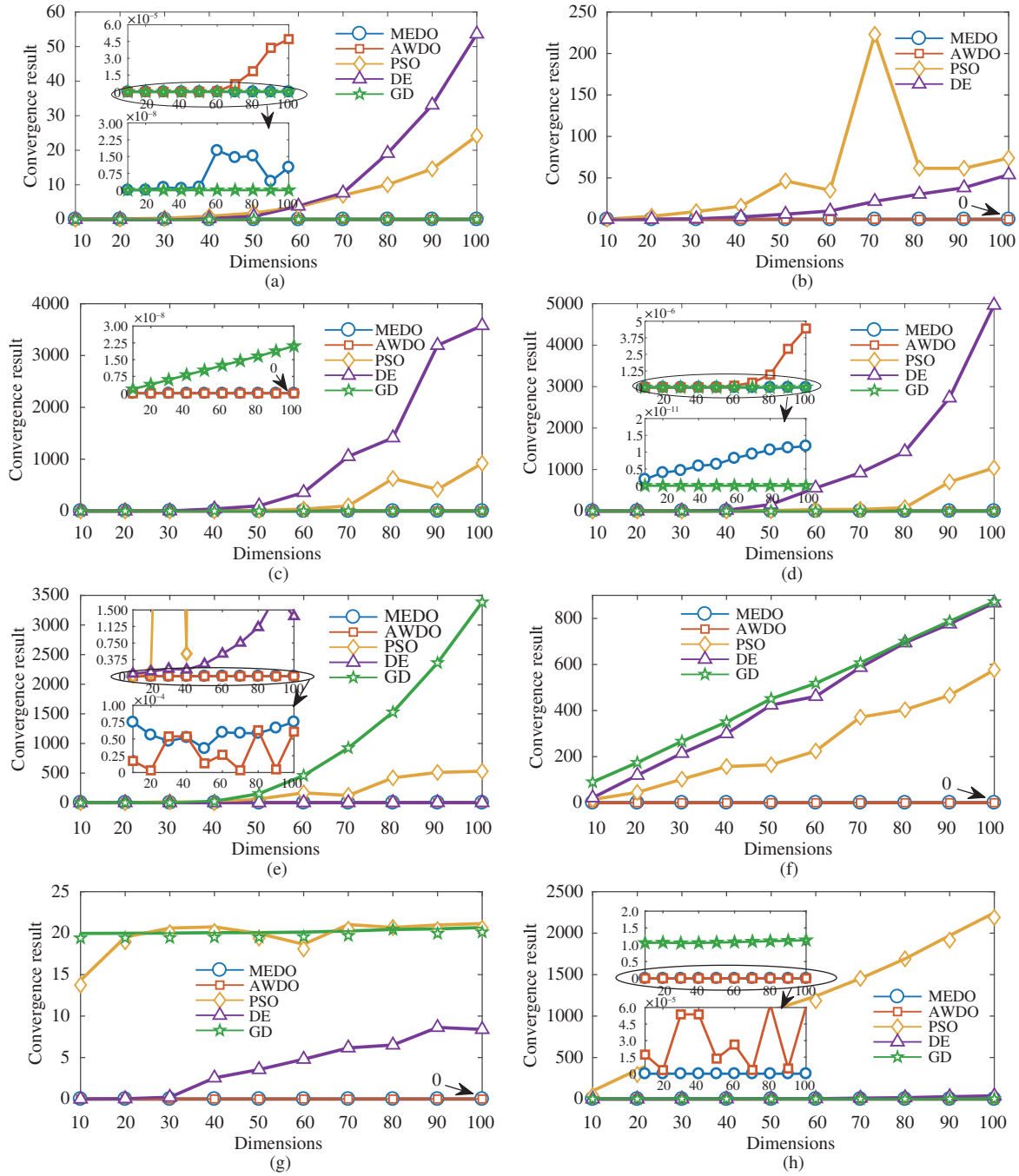
Figure 4 (Color online) Change of the accuracy of different optimizations with the increase of the dimensions when calculating. (a) F_1; (b) F_2; (c) F_3; (d) F_4; (e) F_5; (f) F_6; (g) F_7; (h) F_8.

competitive optimization which can be qualified for the multimodal and high-dimensional questions.

4 Applications in electromagnetics

In this part, four representatives of electromagnetic engineering are selected to demonstrate the advantages of MEDO when it is applied to electromagnetics. These applications are either high-dimensional, or difficult to express directly in analytical form, or extremely multimodal, or with high requirements for stability.
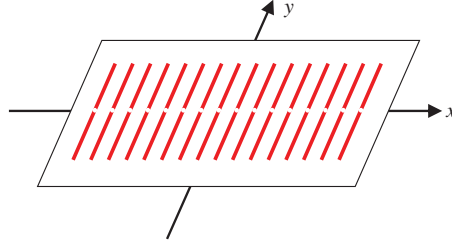
Figure 5 (Color online) Geometry of the 16-elements linear antenna array positioned along the x-axis.

4.1 Linear antenna array synthesis

Antenna array synthesis is one of the most significant optimization problems, including side lobe level (SLL) suppression [31–35], null control [31, 34, 36], and array failure correction [37–39]. It is challenging because of the high-dimensionality and strong-nonlinearity.

4.1.1 *Side lobe level suppression and null control*

In this subsection, MEDO is used to choose the optimal amplitude of the excitation and the element locations to achieve the SLL suppression and null control of a linear array.

The linear array is placed along the x-axis symmetrically, consisting of 16 identical isotropic dipole antennas, as shown in Figure 5. The array factor AF can be calculated as

$$\mathrm{AF}(\theta) = 2 \sum_{n=1}^{16} a_n \cos\left(\frac{2\pi}{\lambda} d_n \cos\theta + \varphi_n\right), \tag{23}$$

where a_n refers to the excitation amplitude of the nth element, d_n refers to the distance between two elements, λ refers to the wavelength, and φ_n refers to the excitation phase of the nth element, respectively. If the phases are preset to be $\pi/2$, Eq. (23) can be simplify as

$$\mathrm{AF}(\theta) = 2 \sum_{n=1}^{16} a_n \cos\left(\frac{2\pi}{\lambda} d_n \cos\theta + \frac{\pi}{2}\right). \tag{24}$$

In order to find the optimal amplitude of the excitation and the location of the elements to achieve a minimal SLL and null control, the objective function is set as

$$f_{\mathrm{objective}} = \max\left(\mathrm{AF}\left(\theta_d\right)\right) + \sum_i \mathrm{AF}\left(\theta_i\right), \tag{25}$$

where θ_d is the angle at which the SLL needs to be controlled. θ_i refers to the direction which needs to control the null depth. If the null control is not considered, the first half of (25) is used.

This case is a 32-dimension optimization problem. MEDO has run 1000 iterations with a population size of 47, where the 5 coefficients are chosen as $B_0 = 8.9\mathrm{E}{-2}$, $\rho S_{\mathrm{bar}} = 1463$, $|g| = 6.84\mathrm{E}{-4}$, $R_1 = 3.7\mathrm{E}{+3}$, $L_2 = 3\mathrm{E}+7$ for SLL suppression, and $B_0 = 0.06$, $\rho S_{\mathrm{bar}} = 300$, $|g| = 1\mathrm{E}-6$, $R_1 = 1\mathrm{E}+3$, $L_2 = 3\mathrm{E}+8$ for null control, respectively.

The similar study has been done by PSO [34] for SLL suppression and by RGA [36] for both SLL suppression and null control. The obtained side lobe levels are shown in Tables 5 and 6. The corresponding normalized far-field patterns are shown in Figures 6 and 7. Table 7 shows the optimal excitations and positions of the elements acquired by MEDO and PSO.

From the results, we can conclude that in the SLL suppression, MEDO can attain a -35.71 dB SLL in the linear antenna array, and PSO achieves -31.29 dB [34]. In the SLL suppression and null control, MEDO can achieve a lower SLL than RGA, with the comparable null depth with the RGA. The consequences show a matched potential to the typical optimizations in minimizing the side lobes level and null control in the antenna array synthesis.

Table 5 Comparison of the SLL obtained by MEDO and PSO

Optimization	SLL (dB)
MEDO	−35.71
PSO	−31.29

Table 6 Comparison of the SLL obtained by MEDO and RGA

Optimization	SLL (dB)	Null depth (75° and 105°) (dB)	Null depth (68° and 112°) (dB)
MEDO	−420.83	−61.65	−61.66
RGA	−15.18	−56.00	−86.07
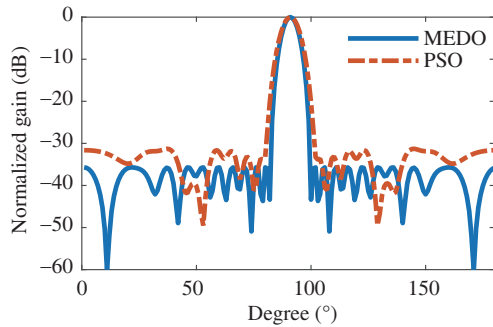
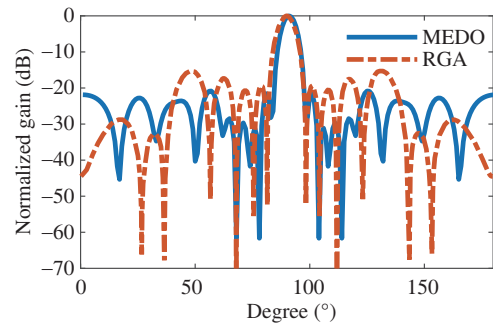**Figure 6** (Color online) Normalized gain comparison between MEDO and PSO. MEDO achieves a lower SLL than PSO.

Figure 7 (Color online) Normalized gain comparison between MEDO and RGA. MEDO achieves a lower SLL than RGA, with the comparable null control in 75°, 105°, 68°, and 112°.

Table 7 Excitation current amplitudes and element positions of 16-element linear array obtained by MEDO and PSO for Subsection 4.1.1

Element number	MEDO (for SLL suppression only)		MEDO (for SLL suppression and null control)		PSO (for SLL suppression only)	
	Excitation amplitude	Position spacing	Excitation amplitude	Position spacing	Excitation amplitude	Position spacing
1st	0.151317	0.62926	0.257102	0.400000	0.210000	0.55053
2nd	0.291622	0.80504	0.310612	0.724125	0.401480	0.66321
3rd	0.468041	0.81434	0.333657	0.650454	0.320900	0.61984
4th	0.584701	0.73644	0.510201	0.559664	0.487930	0.40000
5th	0.564219	0.63420	0.382737	0.529326	0.865320	0.65443
6th	0.69427	0.58506	0.551289	0.550030	1.000000	0.72970
7th	0.719992	0.60010	0.661875	0.574347	0.975160	0.73800
8th	0.595556	0.50668	0.685965	0.703852	0.819060	0.66374
9th	0.777297	0.53528	0.713194	0.708551	0.647310	0.59657
10th	0.762435	0.63004	0.713019	0.689588	0.637890	0.61989
11th	0.710614	0.63960	0.527354	0.666631	0.503760	0.72864
12th	0.629917	0.67286	0.618191	0.655562	0.270990	0.69000
13th	0.435429	0.68788	0.321751	0.532389	0.178350	0.60816
14th	0.330503	0.65466	0.267579	0.444508	0.067443	0.64391
15th	0.213359	0.68206	0.450657	0.715799	0.049728	0.73366
16th	0.136245	0.67226	0.423021	0.809753	0.024616	0.82829

4.1.2 *Array failure correction*

The performance of the array antenna is seriously affected by each element. Once one or more elements in the array are failure, it may lead to a sharp variation of the radiation pattern. However, in many situations like satellites and ships, the replacement of failure elements is difficult. As a result, it is necessary to
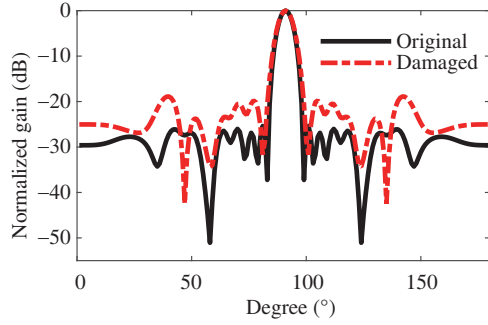
Figure 8 (Color online) Display of the damaged pattern of a 20-elements linear antenna array with the 3rd and the 5th elements are defective.
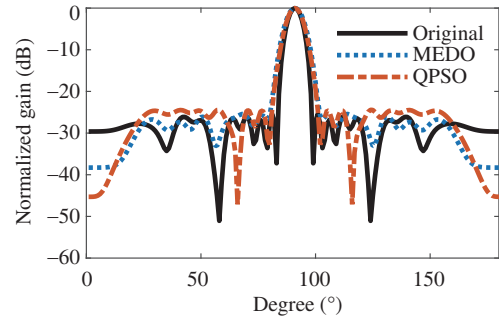

Figure 9 (Color online) Comparison between the original radiation pattern and the correction results by MEDO and QPSO. MEDO can attain a matched performance with QPSO.

Table 8 Excitation current amplitude distribution for original and corrected pattern of MEDO and QPSO

Element number	Original pattern	Corrected pattern by MEDO	Corrected pattern by QPSO
1st	0.2769	0.01	0.1741
2nd	0.3087	0.035661	0.1523
3rd	0.4087	**0**	**0**
4th	0.2993	0.151105	0.3372
5th	0.5075	**0**	**0**
6th	0.5807	0.2104	0.2692
7th	0.775	0.25398	0.5821
8th	0.7555	0.257913	0.5638
9th	0.7742	0.5	0.6564
10th	0.7219	0.520421	0.692
11th	0.8832	0.60911	0.8583
12th	0.7731	0.686959	0.7872
13th	0.6126	0.765111	0.864
14th	0.809	0.748587	0.8718
15th	0.5706	0.788953	0.8739
16th	0.5349	0.669952	0.6647
17th	0.5196	0.551261	0.5375
18th	0.3102	0.556071	0.4607
19th	0.2837	0.50677	0.3564
20th	0.1598	0.246381	0.1574

reconstruct the radiation pattern by designing the exactions of the remainder normal elements [37–39]. MEDO is effective to solve this kind of problem because of its strong global search ability.

In this part, a uniformly placed linear array of 20 parallel half-wavelength vertical dipole antennas is considered. The normal excitation current amplitude of each element is calculated in [39] to obtain a desired side lobe level and return loss. We will use the excitation as an original condition of this example. However, if the 3rd and 5th elements of the array are out of work, it will result in a severe distortion between 30°–65° and 115°–150° in the radiation pattern. The radiation patterns of the original and failure array are shown in Figure 8 in black line and red line, respectively.

MEDO is applied here to find an optimal exaction amplitude of the non-defective elements, which can form a new radiation pattern with the maximal similarity with the antenna performance. The maximal iteration is set to be 100, the population size is 60, and the range of the amplitude to optimize is (0,1), respectively. The objective function is expressed as

$$f_{\text{objective}} = \text{SLL}\left(\text{AF}_{\text{origin}}\right) - \text{SLL}\left(\text{AF}_{\text{corrected}}\right). \tag{26}$$

The similar study has been done by quantum particle swarm optimization (QPSO) [39], whose results can be seen in Figure 9. Table 8 shows excitation current amplitudes of the elements including original
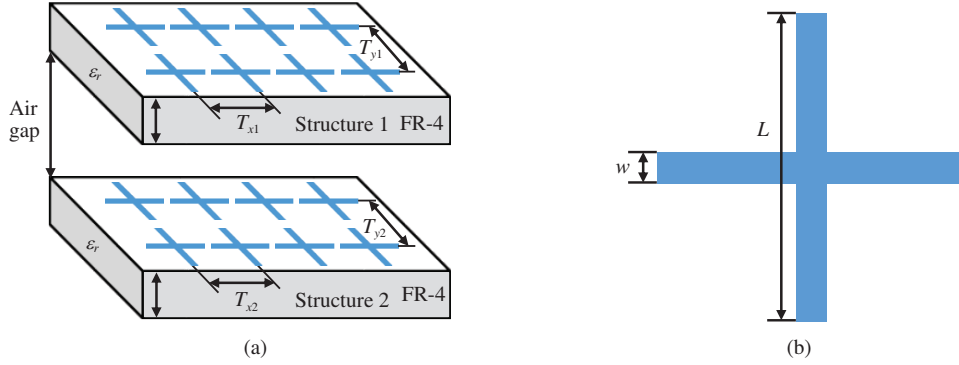
Figure 10 (Color online) Structure of the FSS being designed. (a) Array and (b) crossed dipole element.

Table 9 Parameters of the two-layers FSS structure

Class	Parameter	Value
Substrate	ϵ_r	4.4
	Loss rangent	0.02
Structure 1	L_1	9.87 mm
	w_1	1.35 mm
	h_1	1.57 mm
	T_{x1}	13 mm
	T_{y1}	13 mm
Structure 2	L_2	9.1 mm
	w_2	1.77 mm
	h_2	1.57 mm
	T_{x2}	13 mm
	T_{y2}	13 mm

array, corrected results by MEDO, and corrected results by QPSO.

The result shows a strong consistency between the corrected radiation pattern and the original pattern, which means that MEDO can be qualified to optimize the array failure correction problem.

4.2 Wideband frequency selective surface structures design

Frequency selective surfaces (FSSs) are meta-surfaces which can transmit or reflect the incident electromagnetic wave in a certain range of frequency, acting like spatial filters. A common FSS generally consists of several identical periodic 2-D radiation elements and a dielectric substrate [40]. Crossed dipole is one of the basic types of radiation unit cell that is constantly used in FSS. FSS with crossed dipoles has a good performance in the absorbing of the electromagnetic wave, but still suffers from the limited bandwidth [41]. One of the countermeasures to enhance the bandwidth is to use a multi-layer structure. Properly choosing the gap distance between two layers of the multi-layer FSS, a good balance can be achieved between the bandwidth and insert loss at the resonant frequency [42].

In this subsection, MEDO is applied to optimize the gap distance between two cascaded crossed dipole frequency selective surfaces named structures 1 and 2. The structure of the coupled FSS is shown in Figure 10. The substrate material is FR-4. The gap between two layers is filled by air. More detailed parameters of the coupled FSS can be found in Table 9. Under the above parameters settings, the resonant frequency of the two FSS structures is 9.5 and 10.5 GHz, respectively. The optimization goal is to obtain a wider bandwidth of the coupled FSS structure, and at the same time try not to affect the insert loss at the resonant frequency compared with the single-layer FSS. Thus, the objective function can be expressed as

$$f_{\text{objective}} = S_{21}(9.5 \text{ GHz}) + S_{21}(10.5 \text{ GHz}) + \text{abs}\left(S_{21}(6 \text{ GHz})\right) + \text{abs}\left(S_{21}(12 \text{ GHz})\right), \qquad (27)$$
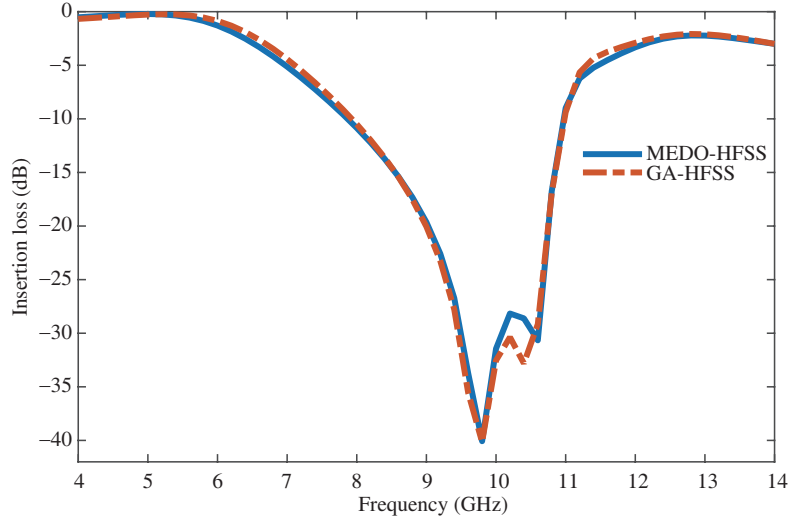
Figure 11 (Color online) Insert loss comparison between MEDO and GA. MEDO can obtain a wider bandwidth than GA.

Table 10 Optimization results comparison between MEDO and GA

	Optimal gap (mm)	Resonant frequency (1) (GHz)	Resonant frequency (2) (GHz)	Bandwidth (−10 dB) (GHz)
MEDO	8.2	9.75	10.53	3.09
GA	7.43	9.73	10.49	3.04

where the value of S_{21} at each frequency point needs to be calculated in conjunction with Ansoft HFSS, which cannot be simply given by the analytical expression.

A population with 47 individuals is optimized for 50 iterations in MEDO, where the following values were used for the coefficients: $B_0 = 0.32$, $\rho S_{\mathrm{bar}} = 320$, $|\boldsymbol{g}| = 0.0025$, $R_1 = 500$, $L_2 = 3\mathrm{E} + 7$. The optimized distance is 8.2 mm, as illustrated in Table 10.

Similar study can also be accomplished by GA [42], whose results are shown in Figure 11 and Table 10. For the sake of fail comparison, we use the data provided in [42] to simulate again with Ansoft HFSS. In consequence, the result of GA is a little different from [42] because of the different electromagnetic software. As can be seen from the results, MEDO can acquire a satisfying bandwidth in the coupled FSS, with 50 MHz (−10 dB) wider than the GA.

4.3 Numerical dispersion reduction for finite-difference method

Finite-difference method (FDM) is a classic numerical method to solve Maxwell's equations [43]. However, it suffers from the numerical dispersion problems seriously because it is developed based on grids [44]. Obtaining the proper coefficients for difference terms of FDM in the concerned frequency can be efficient to reduce numerical dispersion. It is an optimization problem with multimodal.

Under the assumption of the plane wave, the analytical numerical dispersion relationship for the two-dimensional FDM with the 2nd order in time domain and the $2M$th order in spatial domain can be expressed as

$$\cos(\Omega) + \sum_{m=0}^{M} c_m \cos(mK \cos\theta) + \sum_{m=0}^{M} b_m \cos(mK \sin\theta) = 0, \tag{28}$$

where $K = k\Delta x$ refers to the normalized wavenumber, $\Omega = \gamma K = \omega \Delta t$ denotes the normalized frequency, $\gamma = c\frac{\Delta t}{\Delta x}$ is the Courant-Friedirchs-Lewy number, and θ is the propagation angle in the cylinder coordinator system. Therefore, the numerical velocity could be obtained as

$$c_{\mathrm{numerical}}(K) = \frac{c_{\mathrm{real}}}{\gamma K} \arccos\left(-\sum_{m=0}^{M} c_m \cos(mK \cos\theta) - \sum_{m=0}^{M} b_m \cos(mK \sin\theta)\right), \tag{29}$$
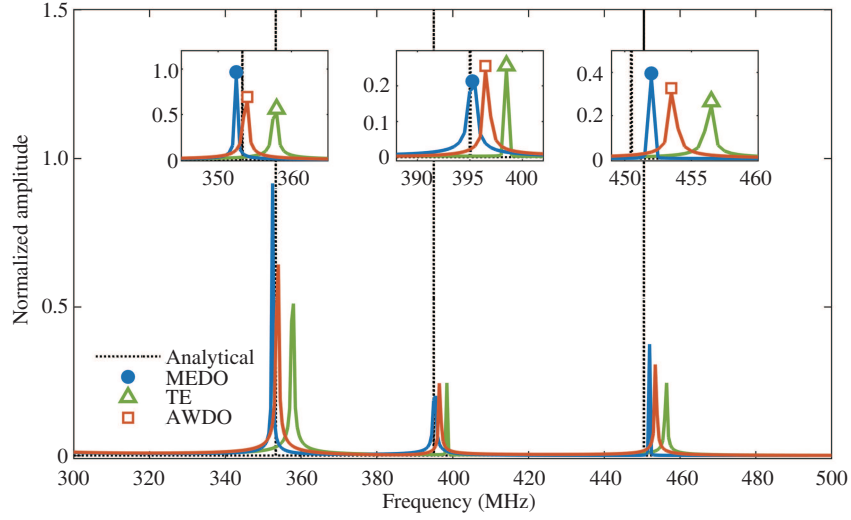
Figure 12 (Color online) Resonant frequency comparison between the TE-based, AWDO-based, and MEDO-based FDM with the analytic results. MEDO-based FDM can obtain a more accurate resonant frequency.

where K and θ are discretized to be a series of values $\{K_i, \theta_i\}_{i=1}^{2M+1}$.

With the ideal coefficients $\{b_m\}$ and $\{c_m\}$, $c_{\text{numerical}}$ should be the same as c_{real} for all K varied from 0 to π and all θ from 0 to $\frac{\pi}{2}$. However, because of the error caused by discretization, $(c_{\text{numerical}} \setminus c_{\text{real}})$ is not always 1. MEDO is applied here to find a series of optimal coefficients $\{b_m\}$ and $\{c_m\}$ that make $(c_{\text{numerical}} \setminus c_{\text{real}})$ as close to 1 as possible. Thus, the objective function is defined as

$$f_{\text{objective}} = \left| \frac{c_{\text{numerical}}}{c_{\text{real}}} - 1 \right|, \tag{30}$$

where $\frac{c_{\text{numerical}}}{c_{\text{real}}}$ is obtained from (29).

To verify the effectiveness of the numerical dispersion reduction method, the FDM with designed coefficients obtained above is used to calculate the resonant frequency of a two-dimensional cavity with perfect electrical conductor boundary condition. The size of the cavity is 120 cm × 120 cm. The excitation source is set to be a Gauss wave $\phi(t) = e^{\frac{-4\pi(t-t_0)^2}{t_c^2}}$, with $t_0 = 0.8t_c = 0.8 \times 10^{-9}$ s. In FDM, $\gamma_x = \gamma_x = 0.6$, $\Delta x = 0.1$ m, $\Delta t = 2 \times 10^{-10}$ s, $M = 2$, and the max time step size is 10000.

Amounts of similar studies have been done in this area, such as TE-based method [45, 46], and optimization methods like AWDO [27].

In MEDO, the population size is 13, and the max iteration number is 200. B_0, ρS_{bar}, $|\boldsymbol{g}|$, R_1, L_2 are valued at 2.3, 298, 0.001, 1934, and 3E + 5, respectively.

The results are shown in Figure 12. It can be concluded that MEDO can converge to a more precise resonant frequency than AWDO. In consequence, MEDO offers another powerful choice in the coefficients optimization process to reduce numerical dispersion.

4.4 Parameters extraction for trapezoidal wave

The trapezoidal wave is widely used as a clock signal in the digital circuits. It often acts as an interference source because of its rich harmonics, which may influence the normal operation of other components. As a result, identifying the trapezoidal wave and extracting its parameters from its emission spectrum are an important work to find the electromagnetic interference (EMI) [47]. In addition, the stability of the parameter extraction method has a great influence on the accurate positioning of EMI [28].

In general, the trapezoidal wave is a periodic signal wave which consists of two triangle waves and one ideal rectangular wave, as shown in Figure 13. There are 6 parameters that need to be used to describe a trapezoidal wave: ω_0, T, E, D_1, D_2, D_3. The parameters denote fundamental angular frequency, time cycle, amplitude, rise time proportion, duty cycle proportion, and fall time proportion, respectively.
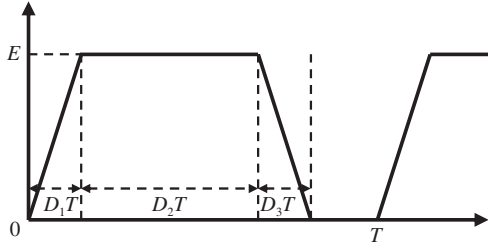
Figure 13 Trapezoidal wave in time domain.
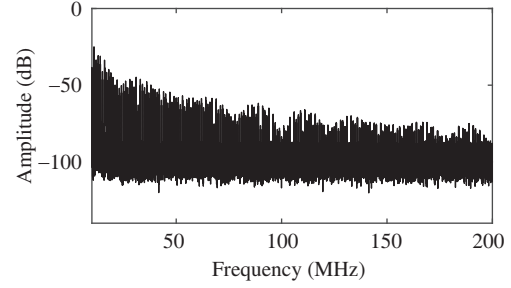
Figure 14 Spectrum from 10 MHz to 200 MHz of the trapezoidal wave.

Among the 6 parameters, fundamental angular frequency ω_0 and time cycle T can be accurately obtained through Lomb-Scargle method [48]. The work in the part is to extract the other three time-domain parameters D_1, D_2, and D_3 from the spectrum of the trapezoidal wave. It can be realized by contrasting the harmonic amplitudes in the spectrum and the harmonic formula that are introduced below.

The positive frequency Fourier series expansion of the trapezoidal wave can be expressed as

$$y(t) = a_0 + \sum_{n=1}^{\infty} |a_n| \cos\left(n\omega_0 t + \angle a_n\right), \tag{31}$$

where $|a_n|$ is the amplitude of each harmonic, shown as

$$\begin{aligned} a_n = -\mathrm{j}\frac{E}{\pi n}\mathrm{e}^{-\frac{\mathrm{j}n\omega_0 T(1.5D_1 + D_2 + 0.5D_3)}{2}} \\ \times \left[Sa\left(\frac{n\omega_0 T D_1}{2}\right) \mathrm{e}^{\frac{\mathrm{j}n\omega_0 T(0.5D_1 + D_2 + 0.5D_3)}{2}} - Sa\left(\frac{n\omega_0 T D_3}{2}\right) \mathrm{e}^{\frac{\mathrm{j}n\omega_0 T(0.5D_1 + D_2 + 0.5D_3)}{2}} \right]. \end{aligned} \tag{32}$$

The objective function to minimize is

$$f_{\text{objective}} = \max_{i=1:N} \left\{ 20\log_{10}\left(\text{abs}\left(\frac{a_i}{a_1}\right)\right) - (A_i - A_1) \right\}, \tag{33}$$

where A_i is the measurement harmonic amplitude of the ith harmonic in dB form, A_1 is the first measurement harmonic amplitude in dB form, a_i is calculated by (31), and N is the total number of sampling.

Optimization algorithms like AWDO [28] are applied to obtain the optimal value of D_1, D_2, and D_3, so as MEDO.

In order to compare the effectiveness and stability of different optimization algorithms to extract time domain parameters, we use a signal generator to generate a trapezoidal wave. D_1, D_2, and D_3 are set to be 0.04, 0.36, and 0.05, respectively, which are the theoretical values of the optimization results. The spectrum data obtained from the spectrum analyzer is shown in Figure 14. Thirteen sample points from 1st to 13th harmonic are selected to extract the time-domain parameters.

In MEDO, the population size is 57, and the max iteration number is 300. B_0, ρS_{bar}, $|\boldsymbol{g}|$, R_1, L_2 are valued at 1.001, 300, 0.0033, 950, 5E + 7, respectively.

To compare the stability of different optimization methods, the simulations with the MEDO and AWDO are repeated 100 times. Table 11 shows the extraction results with the minimum error and the variance of the results for MEDO and AWDO. Figure 15 displays the minimal error of the extraction results for every time.

From Table 11 and Figure 15, we can conclude that MEDO can obtain an optimization result with a comparable accuracy with AWDO, but more stable. Therefore, MEDO is a considerable optimization which can provide a robust result in parameters extraction.

Table 11 Comparison of the parameters extraction results obtained by MEDO and AWDO

Item	Preset value (%)	AWDO		MEDO	
		Best	Variance	Best	Variance
D_1	4.00	3.94	$1.03E-2$	3.94	$3.98E-3$
D_2	36.0	36.1	$1.09E-2$	36.1	$3.96E-3$
D_3	5.00	4.95	$1.09E-2$	4.96	$5.20E-3$
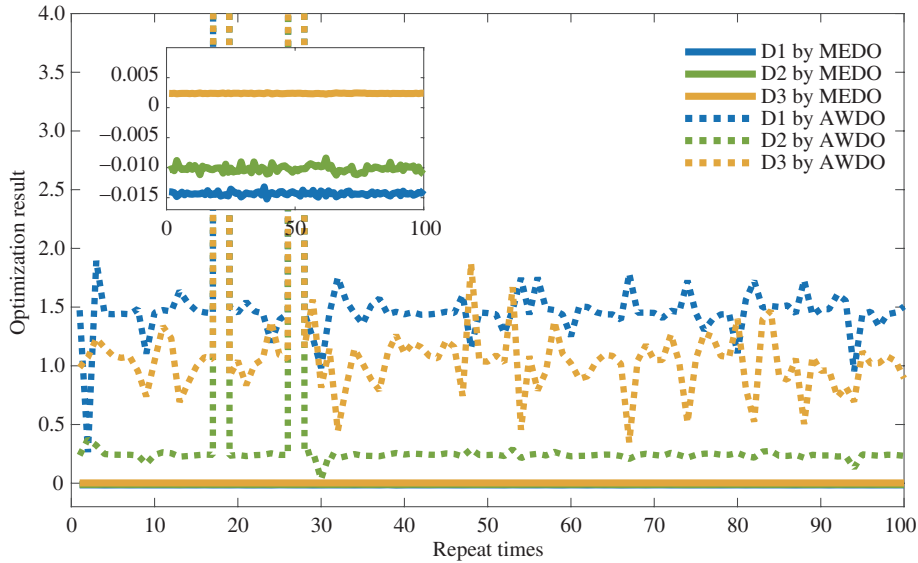
Figure 15 (Color online) Extraction results of D_1, D_2, and D_3 obtained by different optimization algorithms in 100 times.

5 Conclusion

In this paper, a novel global optimization, named MEDO, is proposed. The core idea of MEDO is that constructing an optimization algorithm from the electromagnetic theory may efficiently solve the electromganetic problems, which is presented for the first time. The algorithm transforms the relationship between the variables and the objective function into the positional relationship between two conductors in the parallel circuit. We derived its iterative formula through analyzing the current on the circuit using the Maxwell's equations. Several typical benchmark functions are used to test the accuracy and robustness of MEDO. The results show that MEDO is a stable algorithm and can attain accurate results for both unimodal and multimodal functions. In addition, MEDO is applied to four practical electromagnetic optimization problems, some of which are high dimensional, some have no analytical expressions, some are multimodal, and some require high stability. These examples demonstrate that MEDO is a potential optimization algorithm, and can provide a competitive choice to solve the troublesome optimization problems in electromagnetics. MEDO has also some aspects that need to be improved, admittedly, such as the high time complexity. The work to reduce the time complexity of the proposed MEDO method is in progress, and the related results will be analysed and explained in our future work.

References

1 Baldi P. Gradient descent learning algorithm overview: a general dynamical systems perspective. IEEE Trans Neural Netw, 1995, 6: 182–195

2 Mahony R E, Williamson R C. Prior knowledge and preferential structures in gradient descent learning algorithms. J Machine Learn Res, 2001, 1: 311–355

3 Wu Y M, Jiang L J, Sha W E I, et al. The numerical steepest descent path method for calculating physical optics integrals on smooth conducting quadratic surfaces. IEEE Trans Antenn Propagat, 2013, 61: 4183–4193

4 Xu H J, Huang C Q, Pan P, et al. Image retrieval based on multi-concept detector and semantic correlation. Sci China Inf Sci, 2015, 58: 122104

5 Großhans M, Scheffer T. Solving prediction games with parallel batch gradient descent. In: Proceedings of Joint European Conference on Machine Learning and Knowledge Discovery in Databases, 2015. 152–167

6 Fan Q, Wu W, Zurada J M. Convergence of batch gradient learning with smoothing regularization and adaptive momentum for neural networks. SpringerPlus, 2016, 5: 295

7 Si Z, Wen S, Dong B. NOMA codebook optimization by batch gradient descent. IEEE Access, 2019, 7: 117274

8 Bonnabel S. Stochastic gradient descent on riemannian manifolds. IEEE Trans Automat Contr, 2013, 58: 2217–2229

9 Mercier Q, Poirion F, Désidéri J A. A stochastic multiple gradient descent algorithm. Eur J Oper Res, 2018, 271: 808–817

10 Liu Y, Huangfu W, Zhang H, et al. An efficient stochastic gradient descent algorithm to maximize the coverage of cellular networks. IEEE Trans Wirel Commun, 2019, 18: 3424–3436

11 Tao H, Wu B, Lin X. Budgeted mini-batch parallel gradient descent for support vector machines on spark. In: Proceedings of 2014 20th IEEE International Conference on Parallel and Distributed Systems (ICPADS), 2014. 945–950

12 Ghadimi S, Lan G, Zhang H. Mini-batch stochastic approximation methods for nonconvex stochastic composite optimization. Math Program, 2016, 155: 267–305

13 Khirirat S, Feyzmahdavian H R, Johansson M. Mini-batch gradient descent: faster convergence under data sparsity. In: Proceedings of 2017 IEEE 56th Annual Conference on Decision and Control (CDC), 2017. 2880–2887

14 Eberhart R, Kennedy J. Particle swarm optimization. In: Proceedings of the IEEE International Conference on Neural Networks, 1995. 1942–1948

15 Eberhart R, Kennedy J. A new optimizer using particle swarm theory. In: Proceedings of the 6th International Symposium on Micro Machine and Human Science, Nagoya, 1995. 39–43

16 De Jong K. Adaptive system design: a genetic approach. IEEE Trans Syst Man Cybern, 1980, 10: 566–574

17 Wang Y K, Chen X B. Hybrid quantum particle swarm optimization algorithm and its application. Sci China Inf Sci, 2020, 63: 159201

18 Sun Z X, Song J J, An Y R. Optimization of the head shape of the CRH3 high speed train. Sci China Technol Sci, 2010, 53: 3356–3364

19 Storn R, Price K. Differential evolution—a simple and efficient heuristic for global optimization over continuous spaces. J Glob Optimiz, 1997, 11: 341–359

20 Cui C Y, Jiao Y C, Zhang L, et al. Synthesis of subarrayed monopluse arrays with contiguous elements using a DE algorithm. IEEE Trans Antenn Propagat, 2017, 65: 4340–4345

21 Xiang S, Xing L N, Wang L, et al. Comprehensive learning pigeon-inspired optimization with tabu list. Sci China Inf Sci, 2019, 62: 070208

22 Cui Z H, Zhang J J, Wang Y C, et al. A pigeon-inspired optimization algorithm for many-objective optimization problems. Sci China Inf Sci, 2019, 62: 070212

23 Zhou Y, He F Z, Qiu Y M. Dynamic strategy based parallel ant colony optimization on GPUs for TSPs. Sci China Inf Sci, 2017, 60: 068102

24 Liu H X, Liu F, Zhang X J, et al. Aircraft conflict resolution method based on hybrid ant colony optimization and artificial potential field. Sci China Inf Sci, 2018, 61: 129103

25 Bayraktar Z, Komurcu M, Bossard J A, et al. The wind driven optimization technique and its application in electromagnetics. IEEE Trans Antenn Propagat, 2013, 61: 2745–2757

26 Bayraktar Z, Komurcu M. Adaptive wind driven optimization. In: Proceedings of the 9th EAI International Conference on Bio-inspired Information and Communications Technologies (formerly BIONETICS), 2016. 124–127

27 Chen G, Yang S, Ren Q, et al. Numerical dispersion reduction approach for finite-difference methods. Electron Lett, 2019, 55: 591–593

28 Su D L, Xu H, Zhou Z, et al. An improved method of trapezoidal waves time-domain parameters extraction from EMI spectrum. In: Proceedings of 2019 International Applied Computational Electromagnetics Society Symposium (ACES), 2019. 1–2

29 Paul C R. Inductance: Loop and Partial. Hoboken: John Wiley & Sons, 2011

30 Maxwell J C. A Dynamical Theory of the Electromagnetic Field. London: Royal Society, 1856

31 Bevelacqua P J, Balanis C A. Minimum sidelobe levels for linear arrays. IEEE Trans Antenn Propagat, 2007, 55: 3442–3449

32 Yang S H, Kiang J F. Adjustment of beamwidth and side-lobe level of large phased-arrays using particle swarm optimization technique. IEEE Trans Antenn Propagat, 2014, 62: 138–144

33 Safaai-Jazi A, Stutzman W L. A new low-sidelobe pattern synthesis technique for equally spaced linear arrays. IEEE Trans Antenn Propagat, 2016, 64: 1317–1324

34 Rahman S U, Cao Q, Ahmed M M, et al. Analysis of linear antenna array for minimum side lobe level, half power beamwidth, and nulls control using PSO. J Microw Optoelectron Electromagn Appl, 2017, 16: 577–591

35 Darvish A, Ebrahimzadeh A. Improved fruit-fly optimization algorithm and its applications in antenna arrays synthesis. IEEE Trans Antenn Propagat, 2018, 66: 1756–1766

36 Goswami B, Mandal D. Nulls and side lobe levels control in a time modulated linear antenna array by optimizing excitations and element locations using RGA. J Microw Optoelectron Electromagn Appl, 2013, 12: 238–255

37 Keizer W P M N. Element failure correction for a large monopulse phased array antenna with active amplitude weighting. IEEE Trans Antenn Propagat, 2007, 55: 2211–2218

38 Grewal N S, Rattan M, Patterh M S. A linear antenna array failure correction using firefly algorithm. Progress Electromagn Res M, 2012, 27: 241–254

39 Muralidharan R, Vallavaraj A, Mahanti G K, et al. QPSO for failure correction of linear array of mutually coupled parallel dipole antennas with desired side lobe level and return loss. J King Saud Univ-Eng Sci, 2017, 29: 112–117

40 Munk B A. Frequency Selective Surfaces: Theory and Design. Hoboken: John Wiley & Sons, 2005

41 Kiani G I, Olsson L G, Karlsson A, et al. Cross-dipole bandpass frequency selective surface for energy-saving glass used in buildings. IEEE Trans Antenn Propagat, 2011, 59: 520–525

42 Lins H W C, Barreto E L F, d'Assunção A G. Enhanced wideband performance of coupled frequency selective surfaces using metaheuristics. Microw Opt Technol Lett, 2013, 55: 711–715

43 Yee K. Numerical solution of inital boundary value problems involving Maxwell's equations in isotropic media. IEEE Trans Antenn Propagat, 1966, 14: 302–307

44 Tam C K W, Webb J C. Dispersion-relation-preserving finite difference schemes for computational acoustics. J Comput Phys, 1993, 107: 262–281

45 Fornberg B. Classroom note: calculation of weights in finite difference formulas. SIAM Rev, 1998, 40: 685–691

46 Du Q, Li B, Hou B. Numerical modeling of seismic wavefields in transversely isotropic media with a compact staggered-grid finite difference scheme. Appl Geophys, 2009, 6: 42–49

47 Su D L, Xie S, Chen A, et al. Basic emission waveform theory: a novel interpretation and source identification method for electromagnetic emission of complex systems. IEEE Trans Electromagn Compat, 2018, 60: 1330–1339

48 Shang X, Su D L. Use modified lomb-scargle method to analyze electromagnetic emission spectrum. In: Proceedings of 2015 IEEE 6th International Symposium on Microwave, Antenna, Propagation, and EMC Technologies (MAPE), 2015. 415–420

Profile of Donglin SU

Prof. Donglin SU received the B.E. and M.E. degrees of electromagnetic field and microwave technology, and Ph.D. degree of communication and information system from Beihang University, Beijing, China, in 1983, 1986, and 1999, respectively. From 1996 to 1998, she was a visiting scholar in the Department of Electrical Engineering, University of California, Los Angeles (UCLA). She currently is a professor in the Frontier Institute of Science and Technology Innovation and the School of Electronic and Information Engineering, Beihang University.

She has devoted herself to the field of electromagnetic compatibility (EMC) and electromagnetic environment effects for more than thirty years. Her main research interests include electromagnetic field and microwave technology, EMC and electromagnetic environment, and electromagnetic safety. In 2019, she was elected as a member of Chinese Academy of Engineering.

Prof. Su is the director of the Ministry of Industry and Information Technology (MIIT), key lab of Electromagnetic Environment Effect (E3) for Smart System and Equipment at Beihang University. She also has several other professionals. For example, she serves as the chairs of the Expert Committee of the Electromagnetic Environmental Effects of Antennas Chapter of the Chinese Institute of Electronics, Beijing Chapter of the IEEE Antennas and Propagation Society, and the China Committee and Electromagnetic Field Theory and Application Committee of URSI (from 2011). In addition, she is the principle investigator for more than 30 research projects including the Key Basic Research of National Safety, Major Instruments Project of National Natural Science Foundation of China (NSFC), Key Program of NSFC, and many others.

Propose an approach of quantification design on system-level electromagnetic compatibility

Modern complex electronic systems suffer from various serious EMC problems due to shrinking in the platform size, integrating more electronic devices in a single platform, and working in more bandwidth. Therefore, the proper design upon the EMC has become the key factor to successful development of extremely complex electronic and information systems and platforms. To achieve this goal, Prof. Su proposed a quantification design approach which can co-design

the functionality and the EMC of the complex electronic systems. The two key factors, which must be considered to achieve the above goal, are how to quantify the electromagnetic coupling between various systems, and how to coordinate the function performance and the EMC requirements. Prof. Su proposed a mathematical formulation to quantitatively describe the electromagnetic coupling. In addition, she proposed several EMC modeling and boundary design approaches, which can balance the performance and compatibility of complex electronic systems. These original studies can guarantee various electronic systems compatible without performance degeneration.

Put forward the integrated outfield test for EMC

EMC qualification test and evaluation are essential parts to verify the effectiveness of the EMC design. Because the EMC test for large-scale systems cannot be done under all the working conditions at the beginning of this century, large-scale platforms installed numerous electronic systems frequently suffered various EMC problems during the period of usage. To mitigate this problem which those important EMC tests cannot be carried out in the shielded room, Prof. Su put forward the idea of the comprehensive and integrated EMC test for large platforms and systems in the outfield. There are two major difficulties in field test: the first is how to test the weak electromagnetic emissions mixed with background noises; the second is how to test the electromagnetic sensitivity of the bundled cables. Prof. Su proposed a multi-sensor time-frequency joint test approach to eliminate background noises and extract electromagnetic emissions. Moreover, she developed the multi-frequency approach to test electromagnetic sensitivity, which can evaluate the susceptibility of the bundled cables. These original studies have made significant contributions to the EMC qualification test and evaluation of large platforms under all the working conditions.

Develop the EMC dynamic design and evaluation approach

The development of highly integrated and modularized electronic systems brings new challenges to the EMC design. These challenges include four main aspects: how to identify the main electromagnetic emission sources from a large number of electromagnetic emission sources; how to characterize the electromagnetic environment; how to realize the dynamic EMC design; and how to realize different level co-design from module to formation. After fourteen years of continuous exploration, Prof. Su proposed the basic emission waveform theory from the physical properties of different types of emission sources, which can be used to identify the electromagnetic emission sources. In order to characterize the electromagnetic environment, she proposed the electromagnetic environment element set based on the basic emission waveform theory. She also proposed the dynamic electromagnetic modeling and evaluation approach and then solved the EMC design and evaluation problems in the complex electromagnetic environment. Moreover, Prof. Su proposed the accurate identification techniques

of the electromagnetic emission sources based on the basic emission waveform, which can evaluate the EMC of the modularized systems. These original studies have made pioneering contributions to ensuring the successful achievement of multi-level EMC design for advanced equipment platforms.

She is the author or co-author of more than 170 articles in journals, letters, and conferences, including *IEEE Transactions on Electromagnetic Compatibility*, *IEEE Transactions on Antennas and Propagation*, *IEEE Transactions on Microwave Theory and Techniques*, *IEEE Transactions on Power Electronics*, *and IEEE Transactions on Vehicular Technology*. Meanwhile, she has authored 2 books. The theoretical studies have been successfully applied to solving the EMC problems in complex electronic systems. Her studies have been highly recognized, and received many awards, including the National Technology Invention Awards (1st Grade, List 1st) in 2018, the National Scientific and Technological Progress Award (2nd Grade, List 1st) twice in 2007 and 2012, China, and the National Scientific and Technological Progress Award (3rd Grade, List 3rd) in 1992.

Selected publications

- Su D L, Xie S, Dai F, et al. Theory and Methods of Quantification Design on System-Level Electromagnetic Compatibility. Berlin: Springer, 2019
- Su D L, Xie S, Dai F, et al. The Theory and Methods of Quantification Design on System-level Electromagnetic Compatibility (in Chinese). Beijing: National Defense Industry Press, 2015
- Su D L, Xiao Y. The Technology of Active Integrated Antennas (in Chinese). Beijing: National Defense Industry Press, 2011
- Su D L, Xie S, Chen A, et al. Basic emission waveform theory: a novel interpretation and source identification method for electromagnetic emission of complex systems. IEEE Trans Electromagn Compat, 2018, 60: 1330–1339
- Su D L, Zhu K, Xu H, et al. An accurate and efficient approach for high-frequency transformer parameter extraction. Chin J Electron, 2019, 28: 1059–1065
- Su D L, Yang Z, Wu Q. Interpolation strategy for broadband evaluation of characteristic modes. IET Sci Meas Tech, 2018, 12: 865–871
- Su D L, Park J-S, Qian Y X, et al. Waveguide bandpass filter analysis and design using multimode parallel FDTD diakoptics. IEEE Trans Microw Theory Tech, 1999, 47: 867–876
- Chen G, Yang S, Su D L. An accurate three-dimensional FDTD (2,4) method on face-centered cubic grids with low numerical dispersion. IEEE Antenn Wirel Propag Lett, 2019, 18: 1711–1715
- Nie J, Yang S, Su D L. Spherical equivalent dipole array theory and its applications to complex electromagnetic system. IEEE Access, 2019, 7: 111756–111766
- Liu H Y, Su D L, Yao C, et al. Analytically calculate shielding effectiveness of enclosure with horizontal curved edges aperture. Electron Lett, 2017, 53: 1638–1640
- Shang X F, Su D L, Xu H, et al. A noise source impedance extraction method for operating SMPS using modified LISN and simplified calibration procedure. IEEE Trans Power Electron, 2017, 32: 4132–4139
- Wu Q, Su D L. On the broadband reflector-backed dipole antennas with wide beamwidth for the EMC tests of large equipment above 1 GHz. IEEE Trans Electromagn Compat, 2013, 55: 999–1006